Biomedicine & Pharmacotherapy 154 (2022) 113582

Contents lists available at ScienceDirect

Biomedicine & Pharmacotherapy

journal homepage: www.elsevier.com/locate/biopha

Pentamethinium salts suppress key metastatic processes by regulating mitochondrial function and inhibiting dihydroorotate dehydrogenase respiration☆

Jindriska Leischner Fialova [a,b], Katerina Hönigova [a,b], Martina Raudenska [a,b,c], Lucie Miksatkova [d,e], Renata Zobalova [f], Jiri Navratil [a,b], Jana Šmigová [g,h], Taraka Ramji Moturu [i], Tomas Vicar [a,b], Jan Balvan [a,b], Katerina Vesela [d,e], Nikita Abramenko [d,e], Zdenek Kejik [d,e], Robert Kaplanek [d,e], Jaromir Gumulec [a,b], Daniel Rosel [g,h], Pavel Martasek [e], Jan Brábek [g,h], Milan Jakubek [d,e,*], Jiri Neuzil [e,f,j,k,**], Michal Masarik [a,b,d,***]

[a] Department of Physiology, Faculty of Medicine, Masaryk University, Kamenice 5, CZ-625 00 Brno, Czech Republic
[b] Department of Pathological Physiology, Faculty of Medicine, Masaryk University, Kamenice 5, CZ-625 00 Brno, Czech Republic
[c] Department of Chemistry and Biochemistry, Mendel University in Brno, Zemedelska 1, CZ-613 00, Brno, Czech Republic
[d] BIOCEV, First Faculty of Medicine, Charles University, Prumyslova 595, CZ-252 50 Vestec, Czech Republic
[e] Department of Paediatrics and Inherited Metabolic Disorders, First Faculty of Medicine, Charles University and General University Hospital in Prague, Ke Karlovu 455, 120 00 Prague, Czech Republic
[f] Institute of Biotechnology, Czech Academy of Sciences, Prumyslova 595, CZ-252 50 Vestec, Czech Republic
[g] Department of Cell Biology, Charles University, Viničná 7, 128 44 Prague, Czech Republic
[h] Biotechnology and Biomedicine Centre of the Academy of Sciences and Charles University (BIOCEV), Průmyslová 595, 252 42 Vestec u Prahy, Czech Republic
[i] Crop Production and Biostimulation Laboratory, Interfacultary School of Bioengineers, Université libre de Bruxelles, Belgium
[j] School of Pharmacy and Medical Science, Griffith University, Parklands Avenue, Southport 4222 QLD, Australia
[k] Faculty of Science, Charles University, Vinicna 7, Prague 128 44, Czech Republic

ARTICLE INFO

Keywords:
Dihydroorotate dehydrogenase
Metastasis
Mitochondria
Migration
Pentamethinium salts

ABSTRACT

Mitochondria generate energy and building blocks required for cellular growth and function. The notion that mitochondria are not involved in the cancer growth has been challenged in recent years together with the emerging idea of mitochondria as a promising therapeutic target for oncologic diseases. Pentamethinium salts, cyan dyes with positively charged nitrogen on the benzothiazole or indole part of the molecule, were originally designed as mitochondrial probes. In this study, we show that pentamethinium salts have a strong effect on mitochondria, suppressing cancer cell proliferation and migration. This is likely linked to the strong inhibitory effect of the salts on dihydroorotate dehydrogenase (DHODH)-dependent respiration that has a key role in the *de novo* pyrimidine synthesis pathway. We also show that pentamethinium salts cause oxidative stress, redistribution of mitochondria, and a decrease in mitochondria mass. In conclusion, pentamethinium salts present novel anti-cancer agents worthy of further studies.

1. Introduction

In spite of unprecedented progress in molecular medicine in oncology including the recent discovery and application of immune checkpoint inhibitors [1], cancer is still a considerable challenge, in particular its metastatic form [2,3]. Therefore, it is imperative to search

☆ Dedicated to Prof. Vladimír Král and Dr. Tomáš Bříza

* Corresponding author at: BIOCEV, First Faculty of Medicine, Charles University, Prumyslova 595, CZ-252 50 Vestec, Czech Republic.
** Corresponding author at: Institute of Biotechnology, Czech Academy of Sciences, Prumyslova 595, CZ-252 50 Vestec, Czech Republic.
*** Correspondence to: Department of Physiology and Pathological Physiology, Faculty of Medicine, Masaryk University, Kamenice 5, CZ-625 00 Brno, Czech Republic.
E-mail addresses: milan.jakubek@lf1.cuni.cz (M. Jakubek), jiri.neuzil@ibt.cas.cz (J. Neuzil), masarik@med.muni.cz (M. Masarik).

https://doi.org/10.1016/j.biopha.2022.113582
Received 28 June 2022; Received in revised form 16 August 2022; Accepted 17 August 2022
Available online 30 August 2022

for novel approaches to cancer management that could be utilized for selective and efficient cancer therapy, including intervention in the context of metastatic disease.

Among emerging targets for cancer therapy that has not been yet fully explored and that offers a plausible option for efficient anti-cancer intervention are mitochondria. These organelles differ between cancer and non-malignant cells in a number of properties [4,5] that endow them with the propensity to act as selective targets for cancer therapy for a range of agents [6]. A potential vulnerability of cancer cells via mitochondrial targeting is related to the role of the organelles in energy provision, although it is becoming apparent that the plasticity of cancer cells allows them to switch to non-mitochondrial sources of energy [7–9]. Recent research clearly points to a critical function of mitochondria in metabolism [8], including the provision of precursors for a variety of anabolic pathways [10–12], which makes cancer cell metabolism a thus far under-utilized cancer vulnerability [12,13]. Mitochondria are also essential for metastatic disease [14,15], and we and others have shown that cancer cells with 'fitter' mitochondria are more likely to give rise to metastases [16,17].

To date, there have been a few of anti-cancer agents targeting mitochondria that are used clinically or that are under clinical trials. Of these, the BH3 mimetic venetoclax is used against acute myeloid leukaemia [18]. Of high therapeutic potential is targeting components of oxidative phosphorylation, such as the respiratory complex I that leads to generation of high levels of toxic reactive oxygen species [19,20]. An intriguing mitochondrial target for potential broad-spectrum cancer treatment is an enzyme of the inner mitochondrial membrane dihydroorotate dehydrogenase (DHODH) catalysing the 'mitochondrial step' of *de novo* pyrimidine synthesis required for cell cycle transition of fast proliferating cells [21] and a potential broad spectrum target for cancer therapy [22–24].

We have recently synthetized and tested as mitochondrial probes pentamethinium salts (PMS) that accumulate in the inner mitochondrial membrane thanks to their affinity for cardiolipin and that exert toxicity towards cancer cells [25,26]. Given the notion of mitochondria as emerging target for cancer therapy and given the fact that PMS accumulate in mitochondria, we decided to study anti-cancer efficacy of these agents in more detail. Here, we show that these agents have a considerable impact on mitochondria, which translates into their anti-cancer effect. Molecular docking and biochemical studies show that PMS compounds have high affinity for DHODH and suppress DHODH-dependent respiration. Together with the finding of suppressing migration of cancer cells, our data point to PMS compounds as potential clinically relevant anti-cancer agents.

2. Material and methods

2.1. Synthesis of PMS1

The mixture of 2-(4-pyridyl)malondialdehyde (150 mg, 1.0 mmol), 2-methyl-3-propyl benzothiazolium iodide (640 mg, 20.1 mmol) and dry n-butanol (25 ml) was stirred at 110 °C for 18 h. After cooling to room temperature, the mixture was filtered. The solid was washed with ethanol (3 ×5 ml) and dried in vacuum. PMS1 was obtained as green powder, 498 mg, 79%. ^{1}H NMR (300 MHz, DMSO-d_6, 25 °C): 8.94 (2 H, d, $J = 6.4$ Hz), 8.14–7.80 (8 H, m), 7.60 (2 H, t, $J = 8.2$ Hz), 7.46 (2 H, t, $J = 7.6$ Hz), 6.20 (2 H, d, $J = 13.8$ Hz), 4.28 (4 H, bs), 1.71 (4 H, sextet, $J = 7.0$ Hz), 0.85 (6 H, t, $J = 7.0$ Hz). ^{13}C NMR (126 MHz, DMSO-d_6, 25 °C): 165.9, 148.2, 143.6, 141.3, 128.2, 127.1, 125.5, 123.2, 114.0, 98.3, 47.5, 20.9, 10.8. HRMS $[M]^+$ (m/z) for $C_{30}H_{30}N_3S_2$, calculated: 496.1876, found: 496.1879. Elemental Analysis for $C_{30}H_{30}IN_3S_2$ calculated: C, 57.78; H, 4.85; N, 6.74; found: C, 57.59; H, 4.93; N, 6.67.

2.2. Synthesis of PMS2

The mixture of quaternary salt (1600 mg, 4.86 mmol), malondialdehyde (353 mg, 2.37 mmol), dry butanol (30 ml) and three drops of triethylamine was heated to 110 °C for 18 h. After this period, the mixture was cooled to room temperature and evaporated to dryness. The product was separated by column chromatography (eluent: chloroform/methanol 10:1, silica gel 5 × 30 cm). The product was separated as a deep blue band. Separated fraction was evaporated to dryness and to the rest, ethyl acetate was added and the whole mixture was sonicated for 2 min. The pure product was separated by filtration. The yield was 347 mg, 80% in a form of deep green powder.

^{1}H NMR (300 MHz, DMSO-d_6, 25 °C): 8.78 (2 H, d, $J = 5.6$ Hz), 8.50 (2 H, d, $J = 14.3$ Hz), 7.67 (2 H, d, $J = 7.4$ Hz), 7.46–7.24 (8 H, m), 5.59 (2 H, d, $J = 14.4$ Hz), 3.77 (4 H, t, $J = 6.7$ Hz), 1.75 (12 H, s), 1.55 (4 H, sextet, $J = 7.4$ Hz), 0.74 (6 H, t, $J = 7.3$ Hz); ^{13}C NMR (126 MHz, DMSO-d_6, 25 °C): 173.3, 151.7, 150.4, 144.0, 142.0, 141.2, 131.1, 128.5, 125.3, 125.2, 122.6, 111.5, 100.7, 49.2, 45.0, 27.0, 20.2, 11.0; HRMS $[M]^+$ (m/z) for $C_{36}H_{42}N_3$ calculated: 516.3373, found: 516.3377. Elemental Analysis for $C_{36}H_{42}N_3$ calculated: C, 67.18; H, 6.58; N, 6.53; found: C, 67.32; H, 6.51; N, 6.74.

For the scheme of the synthesis see Fig. S1. Detailed synthesis is described in Bříza et al. [26].

2.3. Cell cultures

Five cell lines PNT1A, PC-3, U-2 OS, 4T1, and Caki-1 were used in the experiments. The PNT1A human cell line was established from normal adult prostatic epithelial cells immortalized by transfection with a plasmid containing the SV40 antigen with defective replication origin. PNT1A cell line (ECAC 95012614) was purchased from the European Collection of Authenticated Cell Cultures (ECACC) and the cells were maintained in RPMI-1640 medium supplemented with 10% FBS, 100 U/ml penicillin and 0.1 mg/ml streptomycin. The PC-3 cell line was established from the grade 4 prostatic adenocarcinoma and derived from the metastatic site in bones. The PC-3 cell line (ECACC 90112714) was purchased from ECACC and maintained in Ham's F12 medium supplemented with 10% FBS, 100 U/ml penicillin and 0.1 mg/ml streptomycin. U-2 OS human osteosarcoma cells were purchased from American Type Culture Collection (ATCC; HTB-96™) and maintained in ATCC-modified McCoy's 5 A medium supplemented with 10% FBS, 100 U/ml penicillin and 0.1 mg/ml streptomycin. Caki-1 cell line was established from a metastatic site (skin) in a 49-year-old Caucasian male with clear cell renal carcinoma. The Caki-1 cell line was purchased from ATCC (HTB-46) and maintained in DMEM with 10% FBS and 100 U/ml penicillin and 0.1 mg/ml streptomycin. 4T1 mouse cancer cell line was also used. The 4T1 cells are murine mammary carcinoma cells (ATCC catalogue no. CRL-2539, 2004). The cells were cultured in RPMI-1640 medium supplemented with 10% FBS, 100 U/ml penicillin, 0.1 mg/ml streptomycin, 1 mM sodium pyruvate, and 4.5 g/l glucose.

Unless stated otherwise, the cells were cultured under standard cultivation conditions in a humidified atmosphere (37 °C, 5% CO_2). RPMI-1640 medium, Ham's F12 medium, fetal bovine serum (FBS), penicillin/streptomycin, trypsin and ethylenediaminetetraacetic acid (EDTA) were purchased from Sigma Aldrich Co. (St. Louis, MO, USA). ATCC-formulated McCoy's 5 A Medium was purchased from ATCC. Phosphate buffered saline (PBS) was purchased from Invitrogen Corp. (Carlsbad, CA, USA).

2.4. Fluorescence microscopy

The intracellular localization of PMS1 and PMS2 was studied by real-time live-cell fluorescence microscopy at 37 °C and in a 5% CO_2 atmosphere. The images were acquired using a confocal fluorescent microscope Leica TCS SP8 WLL SMD FLIM equipped with a water objective HC PL APO CS2 63x (NA 1.2). Cells were seeded on glass-bottom dishes in complete cell culture media and left to adhere for 24 h. Then, the cells were washed twice with PBS and incubated in cell culture media containing the two pentamethinium salts (PMS; 50 nM), respectively. The

localization of PMS1 and PMS2 in mitochondria was confirmed by co-localization with mitochondrial marker MitoTracker Green (MTG; 100 nM). After the incubation with both PMSs and MTG, the cells were washed twice with PBS and subjected to fluorescence microscopy in media without phenol red. The excitation wavelengths were 488 nm (laser power of 9.72 μW) and 640 nm (laser power of 3.25 μW), the emission range was 500–600 nm and 650–750 nm, respectively.

2.5. MTT assay

Cytotoxicity of the two PMSs was determined using MTT assay. Cells were seeded in microtiter plates and cultured under standard cultivation conditions for 48 h to achieve at least 70% confluency. Then, the culture medium was removed and replaced with solution with increasing concentrations of the two PMSs. After another 24 h, the treatment solution was replaced with fresh culture medium containing 5 mg/ml MTT (Sigma-Aldrich, MO, USA) and incubated for 4 h, wrapped in aluminium foil. Then, to dissolve formazan crystals, the medium was replaced with DMSO, and absorbance was immediately determined at 570 nm (Cell plate reader Cytation 3, BioTek, VT, US).

2.6. Colony-forming assay

The antiproliferative potential of the two PMSs was examined using a colony-forming assay. Cells were seeded into a 6-well plate in defined cell concentrations: 1000 cells per well for PNT1A and PC-3 cell lines and 800 cells per well for U-2 OS cell line. After 24 h, the medium was replaced with fresh media containing the two PMSs in concentration 0, 100 or 200 nM. During the incubation period, any shaking or moving with plates was prevented to obtain clear colonies. After 3 weeks, cells were fixed in cold methanol and stained with trypan blue (Sigma-Aldrich, MO, USA). Colony-forming assay images were analyzed using a custom MATLAB script, which consists of image thresholding with manual adjustment of threshold and correction of colony/background areas with manual drawing.

2.7. Measurement of mitochondrial energetics

The effect of pentamethinium salts on mitochondrial respiration was studied by Cell Mito Stress kit on Seahorse Bioscience XF96 analyzer (Seahorse Bioscience, Billerica, MA, USA). All materials for Seahorse measurement were obtained from Agilent technologies (St. Clara, CA, USA). U-2 OS, PC-3, and PNT1A cells were seeded into poly-L-lysine pre-coated 96-well microplate in 200 μl of cell culture media. The cells were incubated for 24 h under standard cultivation conditions and then, fresh media with the two PMSs (concentration 0, 100, 200, 300 and 400 nM) was added. After another 24 h, the medium was replaced by serum-free DMEM containing 5 mM glucose, 1 mM pyruvate and 2 mM glutamine with pH adjusted to 7.4. After incubation at 37 °C without CO_2 for 1 h, the plate was transferred to the analyzer. During the experiment, mitochondrial respiration test was performed by sequential injection of modulators: oligomycin (1 μM), FCCP (1.5 μM) and the combination of rotenone and antimycin A (0.5 μM) [27]. After the measurement, the nuclei were stained by HOECHST 33342 (2 μg/ml) to normalize acquired data to cell number. Results were analyzed by XF Stress Test Report Generators (Agilent Technologies; St. Clara, CA, USA).

2.8. RNA isolation and cDNA preparation

The cells were harvested into micro tubes and washed with PBS and frozen at − 20 °C. TriPure Isolation Reagent (Roche, Basel, Switzerland) was used for RNA isolation as instructed by the manufacturer. RNA samples without reverse transcription were used as a negative control for qRT-PCR to exclude DNA contamination. The isolated RNA was used for the cDNA synthesis. RNA (1000 ng) was transcribed using the Transcriptor First Strand cDNA Synthesis Kit (Roche, Switzerland) according to the manufacturer's instructions. The cDNA (20 μl) prepared from the total RNA was diluted with RNase free water to 100 μl and the amount of 5 μl was analyzed directly.

2.9. Quantitative real-time polymerase chain reaction (qRT-PCR)

The qRT-PCR was performed using TaqMan gene expression assays with the LightCycler®480 II System (Roche, Basel, Switzerland). The amplified DNA was analyzed by the comparative Ct method using ACTB as a reference. The primer and probe sets for ACTB (Hs99999903_m1); MT2A (Hs02379661_g1); BAX (Hs00180269_m1); Bcl-2 (Hs00608023_m1); mTOR (Hs00234508_m1); BIRC5 (Hs00153353-m1); SOX2 (HS01053049_s1); HIF-1α (Hs00153153_m1) were selected from the TaqMan Gene Expression Assays (Life Technologies, USA). The qRT-PCR was performed under following amplification conditions: total volume of 20 μl, initial incubation at 50 °C/2 min followed by denaturation at 95 °C/10 min, then 45 cycles at 95 °C/ 15 s and 60 °C/1 min

2.10. Preparation of samples for confocal microscopy

The cells were seeded on coverslips previously coated with 0,5% gelatin. Cells studied for lipid peroxidation test were stained with Image-iT® Lipid Peroxidation Sensor (Thermo Fisher Scientific, MA, USA) at a final concentration of 10 μM and incubated for 30 min at 37 °C. After incubation, cells were washed with PBS and provided with fresh media. The cells were immediately transferred into a microscopic chamber where they were maintained at 37 °C in a 5% CO_2 atmosphere. Cells studied for mitochondrial fragmentation were incubated with 100 nM of MitoTracker® Red CMXRos (Thermo Fisher Scientific, MA, USA) for 30 min at 37 °C. After incubation, the cells were fixed with 4% formaldehyde in 3% sucrose PBS for 20 min and then permeabilized for 10 min with 0,2% Triton X-100. Fixed-permeabilized cells were incubated in PBS containing 1% BSA for at least 40 min. Then the cells were either incubated with Tom20 antibody (1:200; sc-17764, Santa Cruz Biotechnology, Texas, USA) for 1 h and further incubated with anti-mouse Alexa 488 Fluor™ secondary antibody for 45 min in the dark, or the cells were incubated with fluorophore-conjugated Alexa Fluor™ 488 Phalloidin (A12379, Invitrogen, Massachusetts, USA) for 1 h in the dark. After that, coverslips were washed three times with PBS 0,05% Tween 20 and incubated with DAPI solution (7 μl/50 ml) for 3–5 min to stain nuclei and again washed three times with PBS. Finally, coverslips were mounted onto glass slides with ProLong Gold antifade mounting reagent (Invitrogen, Massachusetts, USA). Images were acquired on a Confocal LSM 880 microscope (Zeiss, Munich, Germany). Bovine serum albumin (BSA), Triton X-100 and Tween were purchased from Sigma-Aldrich, MO, USA.

2.11. Flow cytometry

ROS generation was measured by flow cytometry using a fluorescent dye probe dichlorofluorescein diacetate (DCF-DA, Sigma). This probe is cell-permeable and is hydrolyzed intracellularly to the DCFH carboxylate anion, which is retained in the cell. Two-electron oxidation of DCFH results in the formation of a fluorescent green product dichlorofluorescein (DCF). DCF-DA (stock, 50 mM in DMSO) was added with fresh medium to cell cultures in final concentration 50 μM for 30 min at 37 °C. After incubation time, cells were washed with PBS and centrifuged for 5 min at 450 g, resuspended in PBS, kept on ice, and measured. Previously, cells were treated with a concentration of IC_{50} values of both PMSs for 24 h.

2.12. Molecular docking

The model of DHODH crystal structure complexed with a small molecule inhibitor (3U2O) was acquired from the RCSB Protein Data Bank. Molegro Virtual Docker MVD 7.0.0 was used for docking with

ligands. It uses the MolDock scoring system and is based on a hybrid search algorithm, the so-called controlled differential evolution [28]. This algorithm combines the technique of differential evolution with an algorithm for predicting cavities. The crystal structure of the protein from RCSB PDB was uploaded to the MVD 7.0.0 platform having a built-in cavity detection algorithm that identifies potential binding sites referred to as active sites/cavities. The MolDock Simplex Evolution search algorithm was used [29,30] and the number of runs was 10, with a maximum number of iterations of 2000 for a population size of 50 and an energy threshold of 100. At each step, the smallest "min" Torsion/-translation/rotation was searched, and the lowest energy molecule was preferred. A re-ranking procedure was applied to increase the docking accuracy. Selected ligands were prepared manually using the Chimera V1.15 program [31] and the built-in MVD program. Amino acid residues participating in the 3U2O binding into the largest DHODH cavity were subjected to molecular docking. The grid resolution was set to 0.3 Å. Maximum interactions and maximum population size were set at 1500 and 50, respectively. The resulting docking positions based on the MolDock score were imported and visualized.

2.13. DHODH respiration

DHODH-dependent respiration was carried out as follows. In brief, cells were trypsinized, washed with PBS, resuspended at 2×10^6 cells per ml of the Mir05 medium (0.5 mM EGTA, 3 mM $MgCl_2$, 60 mM K-lactobionate, 20 mM taurine, 10 mM KH_2PO_4, 110 mM sucrose, 1 g/l essentially fatty acid-free bovine serum albumin, 20 mM HEPES, pH 7.1 at 30 °C) and transferred to the chamber of the Oxygraph-2k system (Oroboros Instruments, Austria). Respiration measurements were performed at 37 °C. Cells were permeabilized with 5 μg digitonin per 10^6 cells and a complex I inhibitor (0.3 μM rotenone) was added before the addition of the substrate. DHODH-mediated respiration was assessed by subtracting the residual respiration rate remaining after the addition of 30 μM leflunomide (DHODH inhibitor) from the respiration rate in the presence of 1 mM dihydroorotate (DHO), 3 mM ADP, and 10 μM cytochrome c.

2.14. Atomic Force Microscopy (AFM)

Cells were seeded into 3 cm Petri dishes in low density and incubated for 3 days. After 3 days, the cells were treated with an IC_{50} concentration of PMS1 and PMS2 for 24 h. Then the cells were washed with a medium without FBS and measured on the bio AFM microscope JPK NanoWizard 3 (JPK, Berlin, Germany) placed on the inverted optical microscope Olympus IX-81 (Olympus, Tokyo, Japan) equipped with the fluorescence and confocal module, thus allowing a combined experiment (AFM-optical combined images). The maximal scanning range of the AFM microscope in X-Y-Z range was 100–100-15 μm. The typical approach/retract settings were identical with a 15 μm extend/retract length, setpoint value of 1 nN, a pixel rate of 2048 Hz and a speed of 30 μm/s. The system operated under closed-loop control. After reaching the selected contact force, the cantilever was retracted. The retraction length of 15 μm was sufficient to overcome any adhesion between the tip and the sample and to make sure that the cantilever had been completely retracted from the sample surface. Force-distance (FD) curve was recorded at each point of the cantilever approach/retract movement. AFM measurements were obtained at 37 °C (Petri dish heater, JPK) with force measurements recorded at a pulling speed of 30 μm/s (extension time 0.5 s).

Young's modulus (E) was calculated by fitting the Hertzian-Sneddon model on the FD curves measured as force maps (64 ×64 points) of the region containing either a single cell or multiple cells. JPK data evaluation software was used for the batch processing of measured data. The adjustment of the cantilever position above the sample was carried out under the microscope by controlling the position of the AFM-head by motorized stage equipped with Petri dish heater (JPK) allowing a precise positioning of the sample together with a constant elevated temperature of the sample for the whole period of the experiment. Soft uncoated AFM probes HYDRA-2R-100 N (Applied NanoStructures, Mountain View, CA, USA), i.e. silicon nitride cantilevers with silicon tips are used for stiffness studies because they are maximally gentle to living cells (not causing mechanical stimulation). Moreover, as compared with coated cantilevers, these probes are very stable under elevated temperatures in liquids – thus allowing long-time measurements without nonspecific changes in the measured signal.

2.15. Wound healing assay and spheroid assay

Migrastatic and anti-invasive properties of the two PMSs were assessed using a 2-dimensional (2D) wound healing or scratch assay and a 3D spheroid assay. Wound healing assay was performed on the cell monolayer cultured in fibronectin-coated 12-well plates. A scratch was created using a sterile P200 pipette tip. The released cells were washed with pre-warmed PBS and wells were filled with growth medium with or without added 1 μM PMS1 and PMS2. 3D cell culture spheroids were formed in 2% agarose microwells for 48 h. Each spheroid was embedded in a collagen matrix (1 mg/ml rat tail collagen, 1x RPMI medium, 15 mM HEPES, 1% FBS and 50 μg/ml gentamicin in final composition) and treated with different concentrations (0.625 μM - 5 μM) of PMS1 and PMS2 in the cultivation medium.

The images were acquired using the Leica Thunder system equipped with LAS-X Navigator software module (Leica) and analysed using ImageJ/Fiji software. Manual single-cell tracking was performed on about 50 cells per treatment and replicate using the TrackMate Plugin of ImageJ/Fiji. The spheroid area was delineated using the Threshold or Edge Finder and Binary Mask tool in ImageJ/Fiji software. The invasion index was calculated as a normalized ratio of the spheroid area of interest to the starting spheroid area.

2.16. Real-time impedance-based cell migration and invasion assay

Inhibition of cell motility was measured also with another alternative non-invasive and label-free approach - the impedance-based Real-Time Cell Analysis (RTCA) xCELLigence technology. RTCA xCELLigence system was used according to supplier's (Roche Applied Science and ACEA Biosciences, San Diego, CA, USA) instructions. Cells were deprived of FBS for at least 2 h before the start of the experiment. Half of the wells in CIM-plate 16 was prepared without FBS and into the second half FBS as a chemoattractant was added. Cells were treated with determined IC_{50} values of the PMSs. Attachment and migration of the cells through the microelectrodes was monitored every 15 min. The impedance of electron flow caused by adherent cells was reported using a unitless parameter called Cell Index (CI), where CI = (impedance at time point n – impedance in the absence of cells)/nominal impedance value). To compare between cell lines/treatments, Cell Indices were normalized to value 1.0 at the time 1 h after seeding the cells. Measured data were fitted with non-linear function in statistical software GraphPad Prism.

2.17. Time-lapse holographic microscopy

Quantitative phase imaging (QPI) of the living cells was performed using Q-PHASE, a coherence-controlled holographic microscope, CCHM (TELIGHT, Brno, Czech Republic). The microscopic setup is based on off-axis holography and incorporates a diffraction grating allowing imaging with both spatially and temporally low-coherent illumination leading to high-quality QPI.

After 2 h-observation without treatment the cells were treated with 10 nM concentration of PMS1 or PMS2 and observed for another 22 h in flow chambers μ-Slide I Luer Family (Ibidi, Martinsried, Germany). To maintain ideal cultivation conditions (37 °C, 5% CO2, 60% humidified air) during time-lapse experiments, cells were placed in the gas chamber H201 – for Mad City Labs Z100/Z500 piezo Z-stages (Okolab, Ottaviano,

NA, Italy). To image enough cells in one field of view, Nikon Plan 10/0.30 was chosen. For each treatment, nine fields of view were observed with the frame rate 3 mins/frame.

Holograms were captured by CCD camera (XIMEA MR4021 MC-VELETA). Complete quantitative phase image reconstruction and image processing were performed in Q-PHASE control software. Cell dry mass values were derived according to Prescher and Bertozzi [32] and Park et al. [33] from the phase (Eq. (1)), where m is cell dry mass density (in pg/μm^2), φ is the detected phase (in rad), λ is the wavelength in μm (0.65 μm in Q-PHASE), and α is the specific refraction increment (≈0.18 μm^3/pg). All values in the formula except the φ are constant. The value of φ (Phase) is measured directly by the microscope.

$$m = \frac{\varphi\lambda}{2\pi\alpha} \quad (1)$$

Quantitative phase images were analyzed directly in the microscope's (custom) software (SophiQ).

3. Results

3.1. Pentamethinium salts accumulate in mitochondria of cancer cells

The ability of PMS1 and PMS2 (Fig. 1A) to penetrate the plasma membrane of cancer cells (human cell lines derived from osteosarcoma (U-2 OS) and bone metastasis of prostate cancer (PC-3)) was studied. Both salts crossed the plasma membrane within 5–10 min. To check localization of the salts in mitochondria, we used staining with MTG. The signal of both salts was colocalized with the signal of MTG, confirming that PMS1 and PMS2 selectively accumulate in mitochondria of live U-2 OS and PC-3 cells (Fig. 1B). This was further confirmed by high Pearson correlation coefficient, calculated from the linear correlation of red (PMS 1 and 2) and green (MTG) channels (Fig. 1C).

3.2. Pentamethinium salts affect viability and proliferation of cancer cells

After prolonged exposure to the studied salts, we observed massive cell death in cancer cells. To investigate whether the cytotoxic effect

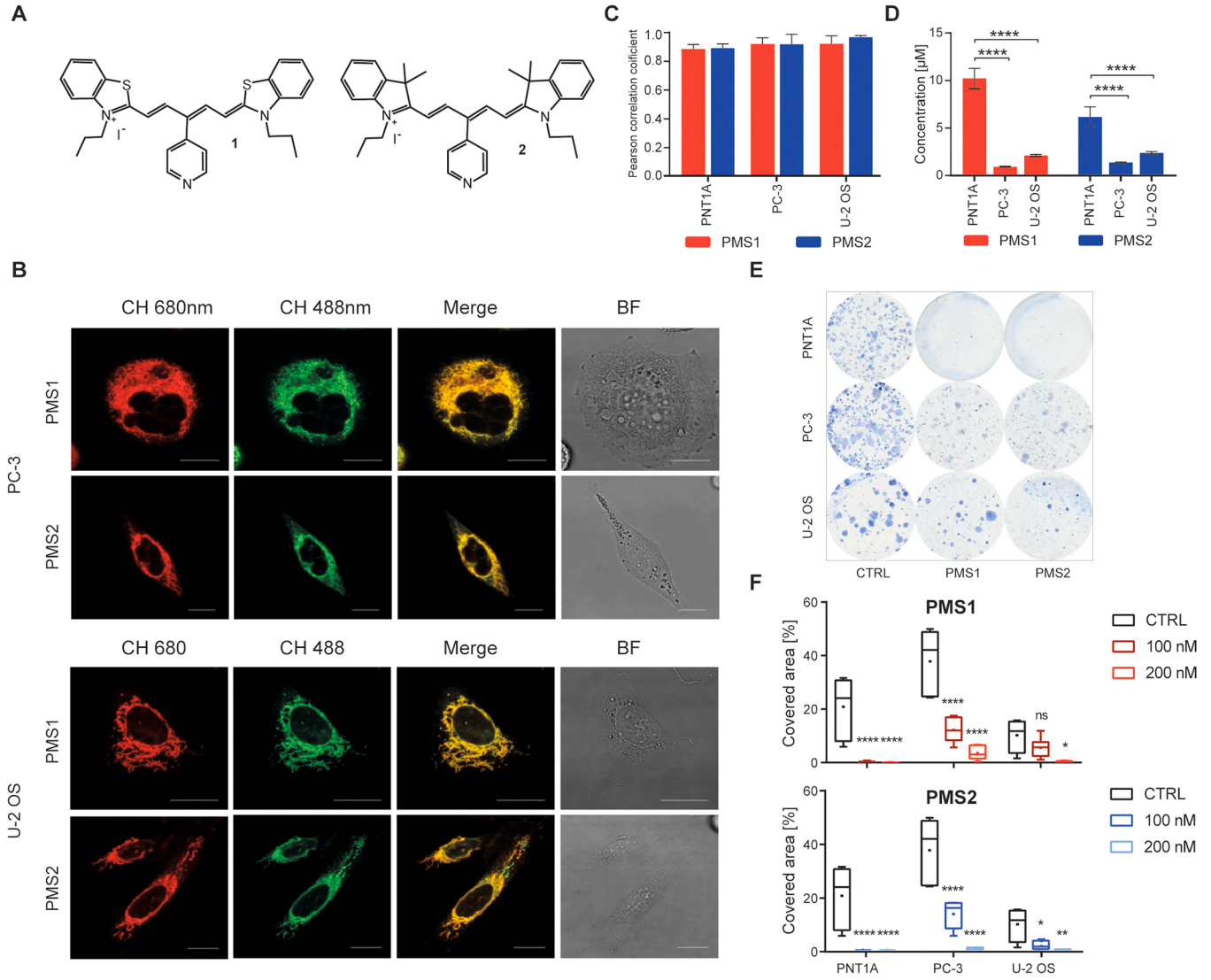

Fig. 1. Pentamethinium salts (PMS), their intracellular localization and antiproliferative effect. A. Chemical structures of γ substituted pentamethinium salts with benzothiazole and indole side unit. **B.** Intracellular localization of PMS1 and 2 in live cells. Top: PC-3 cells, bottom: U-2 OS cells. CH.680nm: Pentamethinium salt (50 nM); CH.488nm: MitoTracker® Green FM (MTG, 100 nM); BF: bright field image. The scale bar represents 20 μm. **C.** High Pearson correlation coefficients of PMS1 and 2 and MTG. **D.** IC_{50} values of PMS1 and PMS2 on PC-3, PNT1A, and U-2 OS cell lines; mean ± SEM, **E.** Colony forming assay. Representative image of colonies stained with Trypan Blue treated with concentration 100 nM of PMS1 and PMS2. **F.** Colony forming results are shown as the percentage of the covered area; min to max plot with median (line) and mean (dot); Two-way ANOVA, * ***: $P < 0.0001$, **: $P < 0.0021$; * : $P < 0.0332$.

could be selective towards cancer cell lines, we included a third cell line, PNT1A, immortalized cells established from normal adult prostate epithelial cells. As shown in Fig. 1C and S5, both PMSs also localize to the mitochondria of PNT1A cells and their penetration through cytoplasmic membrane was similar to those of cancer cells. Using the MTT assay, we determined the IC_{50} values (see Fig. 1D). For U-2 OS cells, we obtained a 4.6-fold higher cytotoxic effect with PMS1 compared to PNT1A cells, with the PC-3 cell line being even more sensitive (IC_{50} = 2.1 μM, 9.7 μM, and 0.9 μM for U-2 OS, PNT1A, and PC-3 cells, respectively). PMS2 had the greatest effect on the metastatic cell line PC-3 with IC_{50} = 1.4 μM, which was 5.9-fold lower than for PNT1A cells. To conclude, both pentamethinium salts showed high specificity towards cancer cells.

To further investigate long term antiprolliferative effects, we used the colony-forming assay. Cells were incubated with the PMSs at 100 nM or 200 nM for three weeks (see Fig. 1E and F). All control cells showed high colony-forming potential, PNT1A cells did not form any colonies after treatment. Although they stayed alive in culture medium, they were no longer attached to the surface (see Fig. S6). Both pentamethinium salts at 100 nM and 200 nM significantly suppressed the colony-forming potential of U-2 OS and PC-3 cancer cells.

3.3. Pentamethinium salts affect mitochondrial electron transport chain, attenuate respiration, and cause oxidative stress

Because pentamethinium salts were designed as mitochondrial probes, we tested how they affect mitochondrial metabolic activity. We investigated mitochondrial respiration and levels of glycolysis using gradually rising concentrations of 100 – 400 nM of PMS1 and PMS2. As shown in Fig. 2A and B, both PMSs caused a drop of mitochondrial oxygen consumption rate (mitoOCR), especially in PC-3 cells, where a significant drop was observed already at 100 nM. U-2 OS cells responded in a concentration-dependent manner. The decrease of mitoOCR was reflected by reduction of mitoATP production. The difference between maximal respiration and basal respiration is referred to as spare respiratory capacity. From the curve obtained during Mito Stress assay (see Fig. 2B and S7), we noticed that not only ATP production, but also the mitochondrial spare respiratory capacity was disturbed by the PMSs, indicating disruption of the electron transport chain (ETC).

All cell lines were able to switch metabolism to glycolysis to substitute for the loss of ATP produced by mitochondria, which is indicated by higher values of extracellular acidification rate (ECAR) in treated cells compared to control cells. The increase in glycolysis and the drop of mitochondrial ATP production was further verified by mitochondrial proton efflux rate (mitoPER) and glycoPER values showing the contribution of mitochondria-derived and glycolysis-derived acidification, respectively. Attenuated respiration was accompanied by increased *SOX2* expression in PTEN-positive cells (PNT1A) (see Fig. 2C). On the other hand, in cells where PTEN expression is reduced (U-2 OS and PC-3 cells), expression of *SOX2* did not significantly change after treatment. The slightly elevated expression of the *HIF-1α* gene was observed in all cell lines after treatment. We also calculated the ratio between genes expression of *BAX* and *Bcl-2* showing the potential sensitivity towards apoptosis, the ratio below 1 indicating a degree of protection against apoptosis. This was achieved only in PNT1A cells, whereas both malignant cell lines, PC-3 and U-2 OS, have the ratio above 1 (see Fig. 2C).

Since mitochondria produce a large portion of intracellular reactive oxygen species (ROS), we were interested in the effect of the PMSs on ROS generation (see Fig. 2D and E). Lipid peroxidation is likely a result of cellular oxidative stress. We tested it using confocal microscopy and the salts at 200 nM. The assay is based on the Image-iT™ Lipid Peroxidation Sensor and expressed as a ratio of its reduced and oxidized forms. In control untreated cells, most of the signal stayed in a red channel and the redox ratio was high (above 5 in PNT1A cells and around 3 in PC-3 and U-2 OS cells (Fig. 2E). After 3 h of treatment, significant increase of oxidation was observed (shown as a drop of redox ratios). Consequently, both PMSs shifted the redox state of the cells towards oxidative stress (except for salt 2 in PC-3 cells). The data are supported by results from flow cytometry using the DCF-DA probe (see Fig. S2). Using this method, we observed massive increase in the signal reflecting ROS levels in cells treated with the PMS1 or PMS2 at concentrations similar to their IC_{50} values. Overall, treatment with both salts disrupts mitochondrial ETC and production of ATP and causes excessive ROS generation.

3.4. Pentamethinium salts bind to DHODH and inhibit DHODH-dependent respiration

Previous results suggest that both pentamethinium salts target the ETC. As mitochondrial complex III oxidizes ubiquinol to ubiquinone, which serves as an electron acceptor for DHODH, we were interested to see whether the salts also target DHODH. To test this hypothesis, we used *in silico* molecular docking and compared the two PMSs with two known DHODH inhibitors. As shown in Fig. 3A and B, both salts can bind to the active site/cavity of DHODH (in green) and the binding is stabilized with two H-bonds in case of PMS1 and one H-bond in case of PMS2. Fig. 3C shows the molecular docking score of two known DHODH inhibitors 03U_1 and BAY2402234 compared with the pentamethinium salts. PMS1 reached the lowest molecular docking score (−170.445 Kcal/mol), suggesting strong binding and high potential to inhibit the enzymatic function of DHODH. Conversely, PMS2 reached the highest molecular docking score (−141.54 Kcal/mol). Nevertheless, the score is close to the 03U_1 inhibitor's score suggesting efficient binding to the polypeptide.

To see whether the *in silico* molecular docking score is also reflected in cells, we conducted a DHODH-dependent respiration assay. We also assessed routine respiration to verify whether the decrease in DHODH respiration is caused specifically by DHODH inhibition or by total depletion of functional OXPHOS. We observed a drop in both types of respiration by using higher doses of the two PMSs. In cancer cells, we observed a reduction of DHODH-dependent respiration at lower concentrations that do not affect routine respiration. The salts did not affect considerably DHODH-dependent respiration in the non-malignant cells. Collectively, these results strongly point to the PMS compounds as inhibitors of DHODH-dependent respiration via their strong affinity for the DHODH polypeptide. (Fig. 3D-G). The inhibitory effect seems to be cell line-dependent (higher in U-2 OS than in PC-3).

3.5. Pentamethinium salts cause a decrease and redistribution of mitochondrial mass and a drop in cell stiffness

We used the mitochondrial probe MitoTracker Red to see functional mitochondria as the intensity of MitoTracker Red changes along with membrane potential. After application of the PMSs, mitochondrial activity was attenuated, and the number of active mitochondria was reduced (see Fig. 4A-E). Disruption of the mitochondrial network was also observed by staining of mitochondria with the Tom20 antibody. In addition, both PMSs caused translocation of mitochondria from the leading edge of the cell to the perinuclear compartment, which can affect the ability of cells to migrate (Fig. 4A). To quantify the mitochondrial network, we used the Fiji plugin Mina, which skeletonizes a 2D image of the mitochondrial network created from the z-stack as shown in Fig. 4B. After 24 h treatment, we found a statistically significant reduction in mitochondrial footprint in all cell lines using both PMSs (see Fig. 4C-E). Mitochondrial footprint normalized to cell area was also significantly changed in all cell lines. The drop in the numbers of mitochondria was also reflected by a drop in the cell stiffness (see Fig. 4F and G). Illustrative microscopic pictures with the heatmap of the cell stiffness are shown in Fig. 4F.

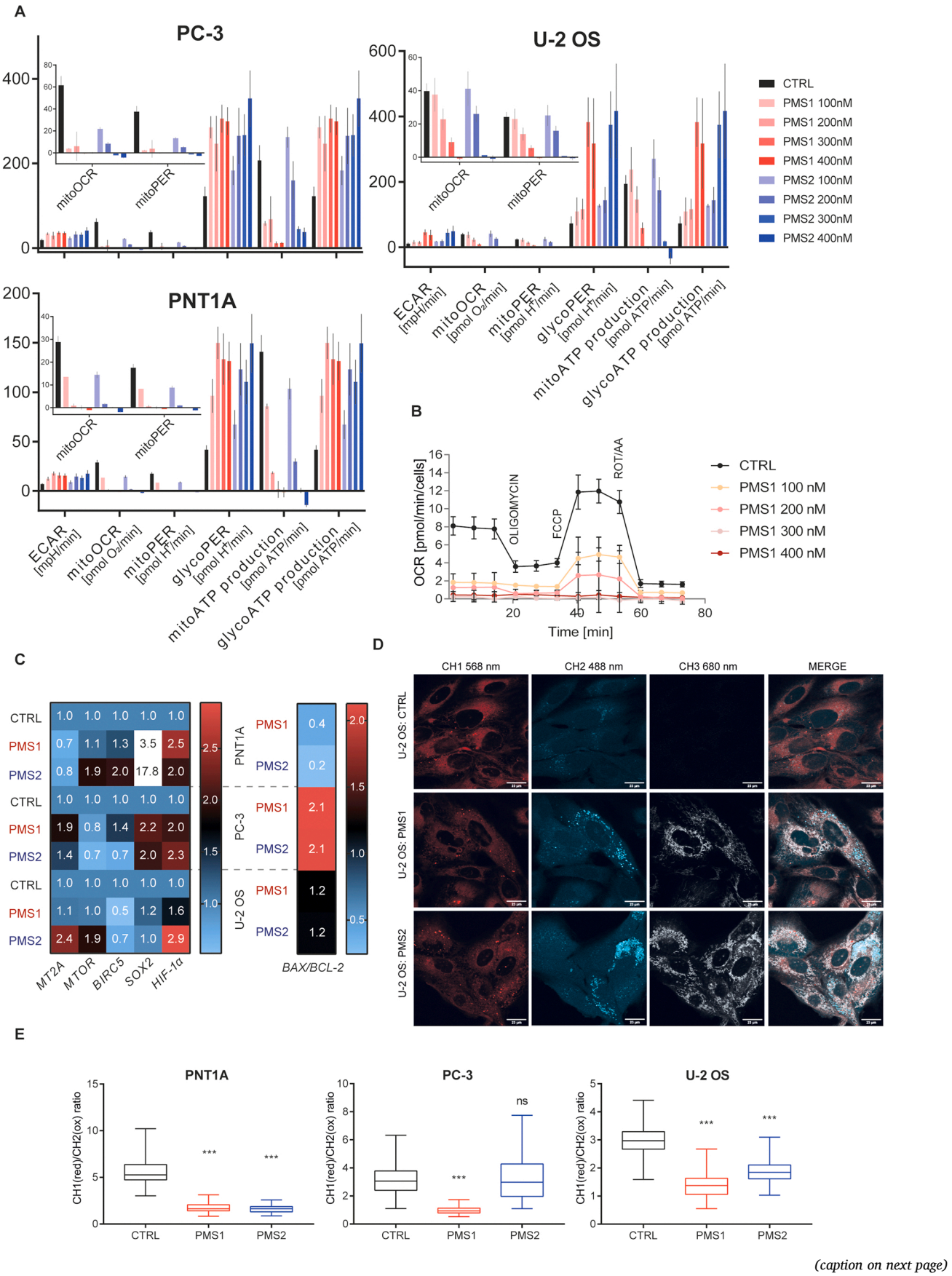

(caption on next page)

Fig. 2. Effects of pentamethinium salts on glycolysis, respiration and oxidative stress. A. Metabolic activity after treatment with tested PMSs. Parameters linked to mitochondrial respiratory activity and glycolysis, namely ECAR, mitoOCR, mitoPER, glycoPER, mitoATP production and glycoATP production. ECAR = extracellular acidification rate; OCR = oxygen consumption rate; PER = proton efflux rate. All cell lines were treated with PMS1 (red) and PMS2 (blue), mean±SD **B.** Real-time measurement of OCR level in PC-3 cells with treatment of PMS1 with the addition of oligomycin, FCCP and ROT/AA; FCCP = carbonyl cyanide-p-trifluoromethoxyphenylhydrazone; ROT/AA = rotenone/antimycin A. **C.** Gene expressions after exposure to 400 nM of the two PMSs. mRNA expression of 7 genes was measured by qRT-PCR and Ct values were normalized to fold change to control cells. The following heatmap shows the ratio calculated from mean fold changes of genes BAX and BCL-2. **D.** Illustrative images of U-2 OS cell line acquired with LSM 880 Zeiss confocal microscope using 63x objective. Cells were stained with Image-iT™ Lipid Peroxidation Sensor. Channel 3 (CH3 680 nm) captured the PMS 1 and 2. **E.** Ratios of signals measured with setting: excitation/emission of 568/591 nm for the red channel and excitation/emission of 488/510 nm for the green channel. The signal was then quantified using CellProfiler software; cells were treated with the concentration of 200 nM of PMSs; mean intensity; min to max plot; Two-way ANOVA, *** : P < 0.001, **: P < 0.01; * : P < 0.05.

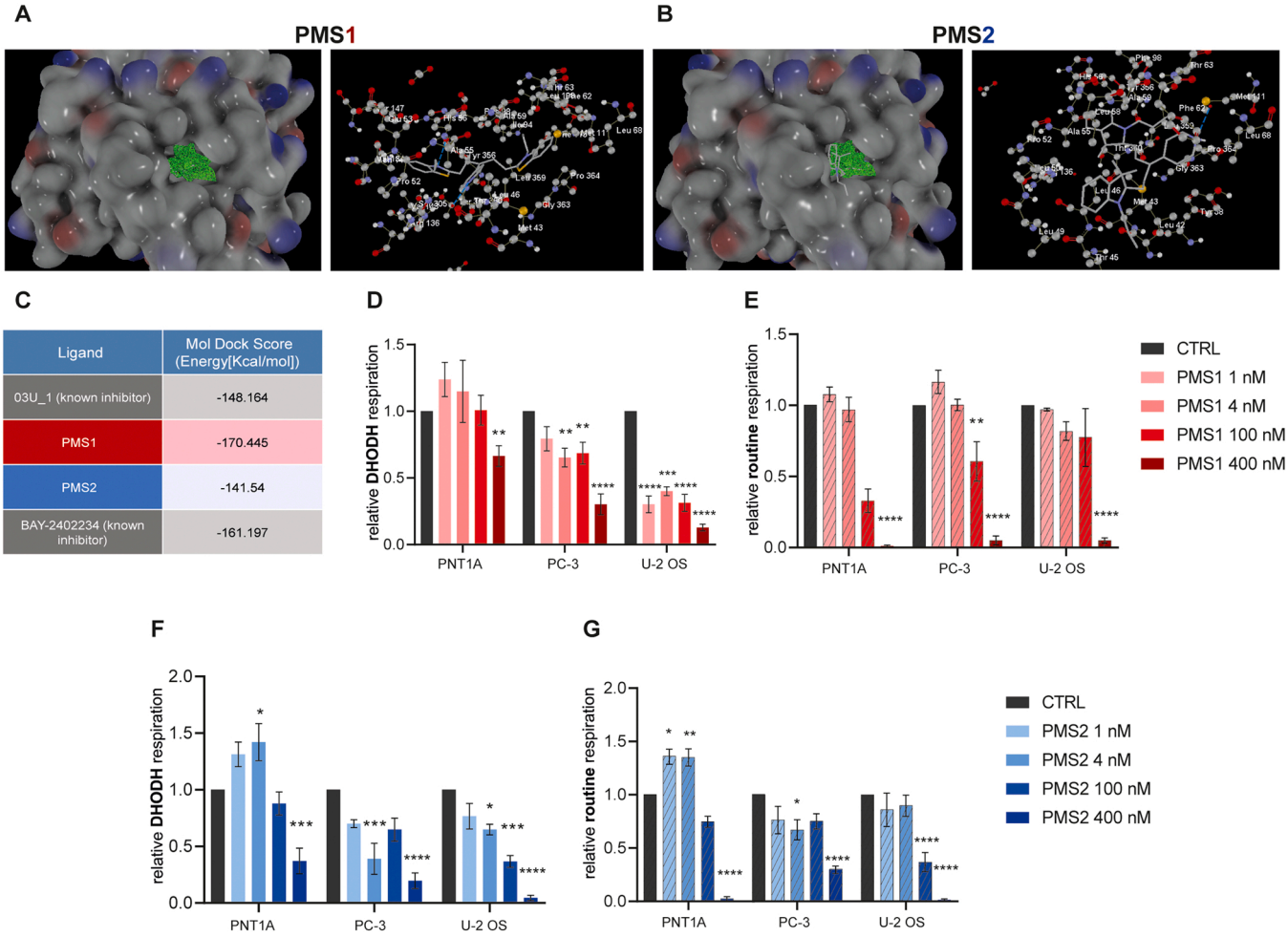

Fig. 3. Molecular docking and DHODH-dependent respiration. **A-B.** Molecular docking of both PMSs as ligands with the protein DHODH. Left: Surface view of DHODH with the active site/cavity (in green) for the ligand 3U2O. Right: Docking of the reference ligand of DHODH and amino acids in the active site/cavity. Blue lines represent the H-bond interactions. **C.** Results of Molecular docking displayed as docking score. Two known inhibitors were used as a reference. **D-G.** DHODH-dependent respiration and routine respiration after treatment with PMS1 (**D, E**) and 2 (**F, G**) with concentrations 1, 4, 100, and 400 nM. Two-way ANOVA, *** : P < 0.001, **: P < 0.01; * : P < 0.05.

3.6. Pentamethinium salts diminish motility, migration, and the invasive potential of cancer cells

Next, we tested the possible migrastatic and anti-invasive effects of PMS1 and PMS2 using the 2D wound-healing assay and the label-free impedance-based real-time cell analysis. In the wound-healing assay analysis (Fig. 5 A), we focused on the migration speed of single cells rather than on wound closure, as the anti-proliferative effect of both pentamethinium salts would affect the wound healing rate. We found that both salts reduce cellular velocity in all cell lines (Fig. 5B). Furthermore, we used the label-free impedance-based real-time cell analysis in two different ways. The migration assay (the first row in Fig. 5C) was performed in wells without any additional layer of substrate to see the ability of cells to migrate through the micropores, whereas for the second approach, we added a layer of Matrigel to analyze the invasion ability of the cells (the second row in Fig. 5C). Cells treated with PMS1 and PMS2 could not invade through the Matrigel layer, and their migration rate was also decreased. Only PC-3 cells were able to effectively migrate after the treatment with PMS2. PMS1 turned out to be the most effective against PC-3 cells, where we observed the greatest inhibitory effect. The highest normalized cell indices achieved under different treatment conditions are shown in the two tables of Fig. 5C.

To confirm our findings regarding anti-migratory properties of the two salts, we performed a quantitative phase imaging (QPI) technique, holographic microscopy. The same fields of view were observed for 2 h in the cell culture medium (control; no PMS added) and 22 h in the

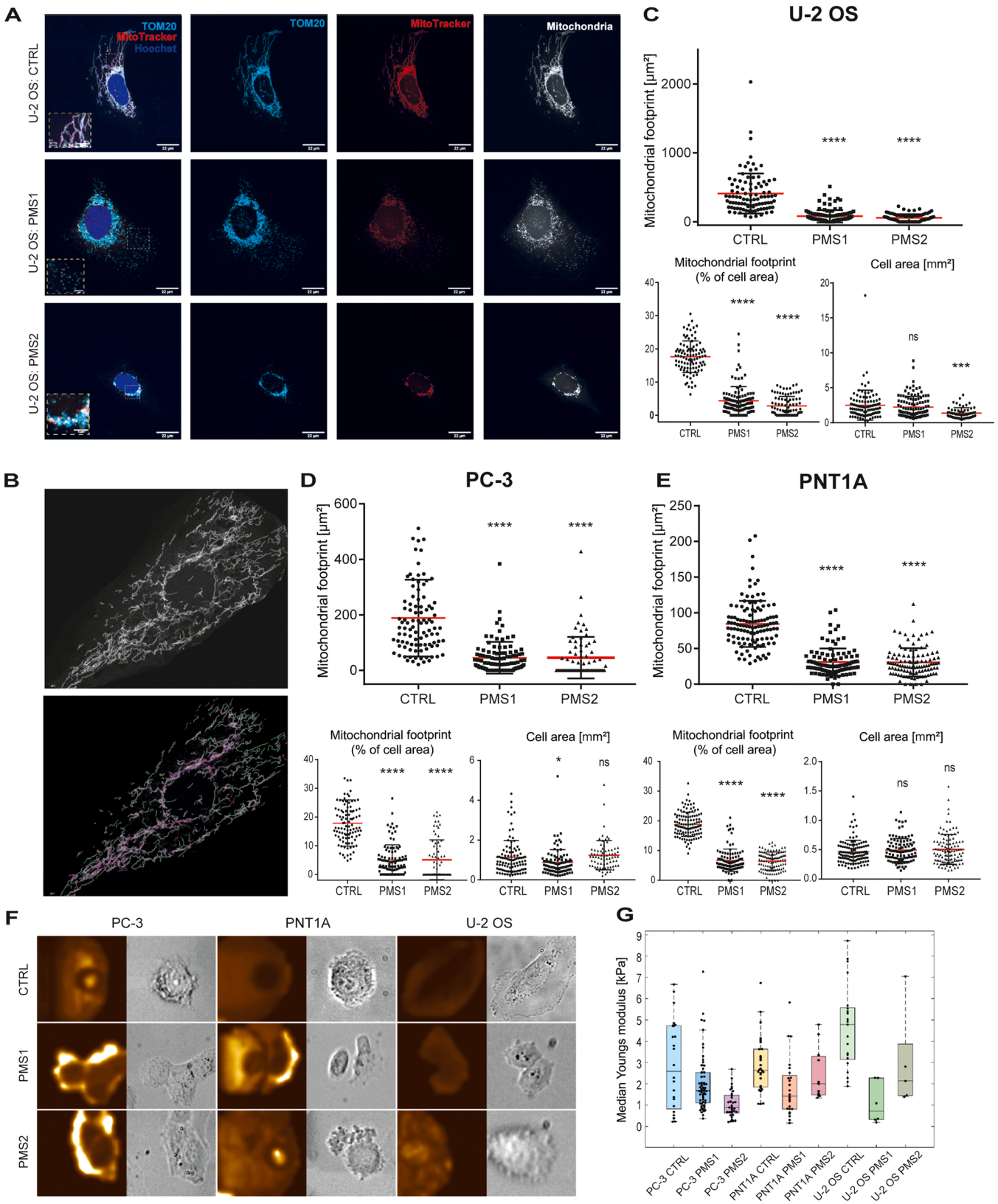

Fig. 4. Effect of pentamethinium salts on mitochondrial network. **A.** Decrease in mitochondrial membrane potential and fragmentation of active mitochondria. Illustrative images of U-2 OS cells acquired with LSM 880 Zeiss confocal microscope using 63x objective. Mitochondria (cyan, red, and white) were stained with Tom20 and MitoTracker ® Red CMXRos. Nuclei are stained with DAPI (blue). Mitochondria stained with MitoTracker are also shown in white to increase visibility. **B.** Representative image of skeletonization and its analysis using the FIJI plugin Mina. **C-E.** Mitochondrial footprint and cell area. Each cell is shown as a single dot in plot graphs, mean (red line). Two-way ANOVA, *** : $P < 0.001$, **: $P < 0.01$; * : $P < 0.05$ **F.** The illustrative microscopic pictures obtained from AFM with the heatmap of the cell stiffness. **G.** Median values of Young's modulus (kPa). Each cell is shown as a single dot in box plot graphs, median is highlighted with a black line.

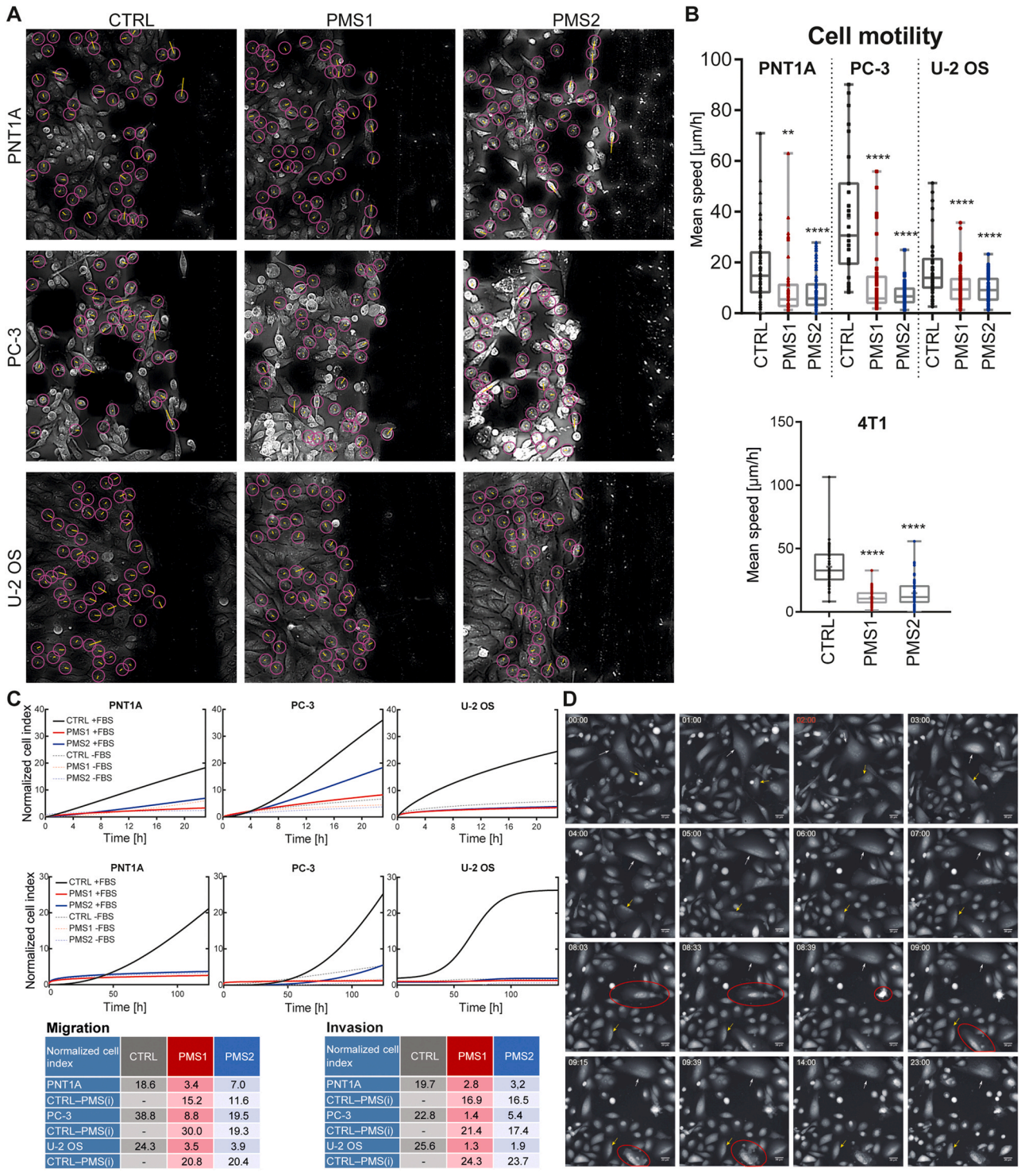

Migration

Normalized cell index	CTRL	PMS1	PMS2
PNT1A	18.6	3.4	7.0
CTRL–PMS(i)	-	15.2	11.6
PC-3	38.8	8.8	19.5
CTRL–PMS(i)	-	30.0	19.3
U-2 OS	24.3	3.5	3.9
CTRL–PMS(i)	-	20.8	20.4

Invasion

Normalized cell index	CTRL	PMS1	PMS2
PNT1A	19.7	2.8	3,2
CTRL–PMS(i)	-	16.9	16.5
PC-3	22.8	1.4	5.4
CTRL–PMS(i)	-	21.4	17.4
U-2 OS	25.6	1.3	1.9
CTRL–PMS(i)	-	24.3	23.7

Fig. 5. Effect of pentamethinium salts on motility, migration, and invasion. **A.** Scratched cell monolayers of U-2 OS, PNT1A, and PC-3 cells without or with 1 μM of PMSs. Images were processed for TrackMate plugin. For cell tracking, the regions with similar local cell densities at time 24 h were used. Cell tracks are depicted as yellow lines. **B.** The box plot graph represents the mean velocity of ~50 cells per condition at time 24 h. Two-way ANOVA, *** : $P < 0.001$, **: $P < 0.01$; * : $P < 0.05$ **C.** Real-time impedance-based cell migration and invasion assay. All cell lines treated with IC_{50} concentration of both PMSs. Cells were monitored for 24 h to monitor cell migration (first row). Cells were monitored for at least 125 h to monitor cell invasion (second row, MatriGel layer added). Cells stimulated with the chemoattractant (FBS) are shown with a solid line, negative controls without a chemoattractant with a dashed line. Measured data were fitted with non-linear function. Tables of endpoint values and subtracted values of control versus treated cells show a decrease in cell migration/invasion. **D.** Representative images from the video acquired by QPI holographic microscopy. White and yellow arrows indicate the motion of chosen cells and its direction. During the first 3 h of the experiment, cells moved quickly and often changed direction. Within 2 h after the addition of PMS1 (in this case), the cells decelerated and stabilized their direction of movement. After 12 h, cells stopped their movement completely and at the end of the experiment, most of them had round morphology. Two ongoing cell deaths are captured in the field of view, marked with a red ellipse. The time counter is situated in the upper left corner in hh:mm format and addition of PMS1 is distinguished by red color; 10x magnification.

medium with 10 nM of PMS1 or PMS2. Both PMSs turned out to be highly phototoxic when exposed to light at the wavelength of 650 nm. Therefore, we used a 10 nM concentration that is not fatal within shorter time periods. Consistent with our observations, in the presence of both salts, we detected decrease in speed in all three cell lines even with such low concentration (for all average morphological/dynamical parameters see Table 1). After addition of both PMSs, PC-3 and PNT1A cells demonstrated higher cell mass than controls. Because the growth rate was lower, increase in the cell mass could be the result of intracellular accumulation of tested salts.

Both salts displayed a strong inhibitory effect on the motility of PC-3 cells (a drop from 77 μm/h to 17 μm/h in the case of PMS2; from 181 μm/h* to 27 μm/h in the case of PMS1). Additionally, both substances reduced the growth rate and increased the circularity of cancer cells, which can be a result of ongoing cell death. Indeed, as shown in Fig. 5D, two cells undergoing cell death are marked with red ellipses. The increase of circularity was also observed in U-2 OS cells, but not in PNT1A cells. Increase of circularity can be induced by the loss of contact with the substrate during apoptosis, moreover, the reduction of cell area corresponds with the shrinkage of a cell during the apoptotic process. Fig. 5D illustrates decrease in the movement of the cells. Two cells in Fig. 5D are indicated by white and yellow arrows. The images are taken from the video acquired using the holographic microscope with the time displayed in the upper left corner. The addition of PMS1 is distinguished by the red color of the timer. Representative videos of all cell lines with treatment of PMS1 or PMS2 are available at https://doi.org/10.5281/zenodo.6445603.

To investigate the migrastatic and anti-invasive effect of PMSs in a 3D system, we used the spheroid assay. Since PNT1A and PC-3 cells did not form spheres, we used human renal cancer cell line Caki-1 and mouse breast tumor cell line 4T1. Both salts caused decrease in speed and invasion even in concentration below 1 μM. Due to the higher invasiveness of Caki-1 and 4T1 cells, the anti-invasive properties of pentamethinium salts were even more evident in these cell lines than in U-2 OS cells (see Fig. 6; Fig. S3 and S4).

4. Discussion

Mitochondria play an important role in cancer progression because they meet the metabolic and bioenergetic needs of malignant cells. Mitochondrial shape and function are flexibly adapted to hostile conditions in the tumor microenvironment to support the growth of cancer cells and to evade activation of mitochondria-dependent cell death mechanisms [34,35]. While ATP generation by means of OXPHOS is probably dispensable for tumorigenesis, pyrimidine biosynthesis dependent on the respiration-linked activity of DHODH is required to overcome cell-cycle arrest and enable tumor progression [9]. The highly potent and selective DHODH inhibitor BAY 2402234 was very efficient

Table 1
Morphological/dynamical parameters acquired by QPI.

PMS	Mass (pg/μm^2)	Area (μm^2)	Speed (μm/h)	Growth rate (pg/h)	Perimeter (μm)	Circularity (%)
			PNT1A			
1 (control)	192	412	13	8	82	74
1 (treated)	232	517	11	3	96	69
2 (control)	287	702	24	12	123	58
2 (treated)	300	664	20	-38*	119	58
			PC-3			
PMS	Mass (pg/μm^2)	Area (μm^2)	Speed (μm/h)	Growth rate (pg/h)	Perimeter (μm)	Circularity (%)
1 (control)	473	912	181*	136	138	63
1 (treated)	560	850	27	3	122	72
2 (control)	460	702	77	53	118	66
2 (treated)	544	675	17	-1	106	74
			U-2 OS			
PMS	Mass (pg/μm^2)	Area (μm^2)	Speed (μm/h)	Growth rate (pg/h)	Perimeter (μm)	Circularity (%)
1 (control)	439	1470	22	24	200	51
1 (treated)	365	1317	21	3	174	58
2 (control)	369	1180	25	1*	164	59
2 (treated)	291	1223	16	24*	163	62

In all cell lines the mass, area, speed, growth, perimeter, and circularity parameters were measured before and after treatment with PMS1 and PMS2 and directly calculated in microscope's software. The means of the parameters are displayed. *The extreme values can be a result of mistakes during automatic cell detection and segmentation.

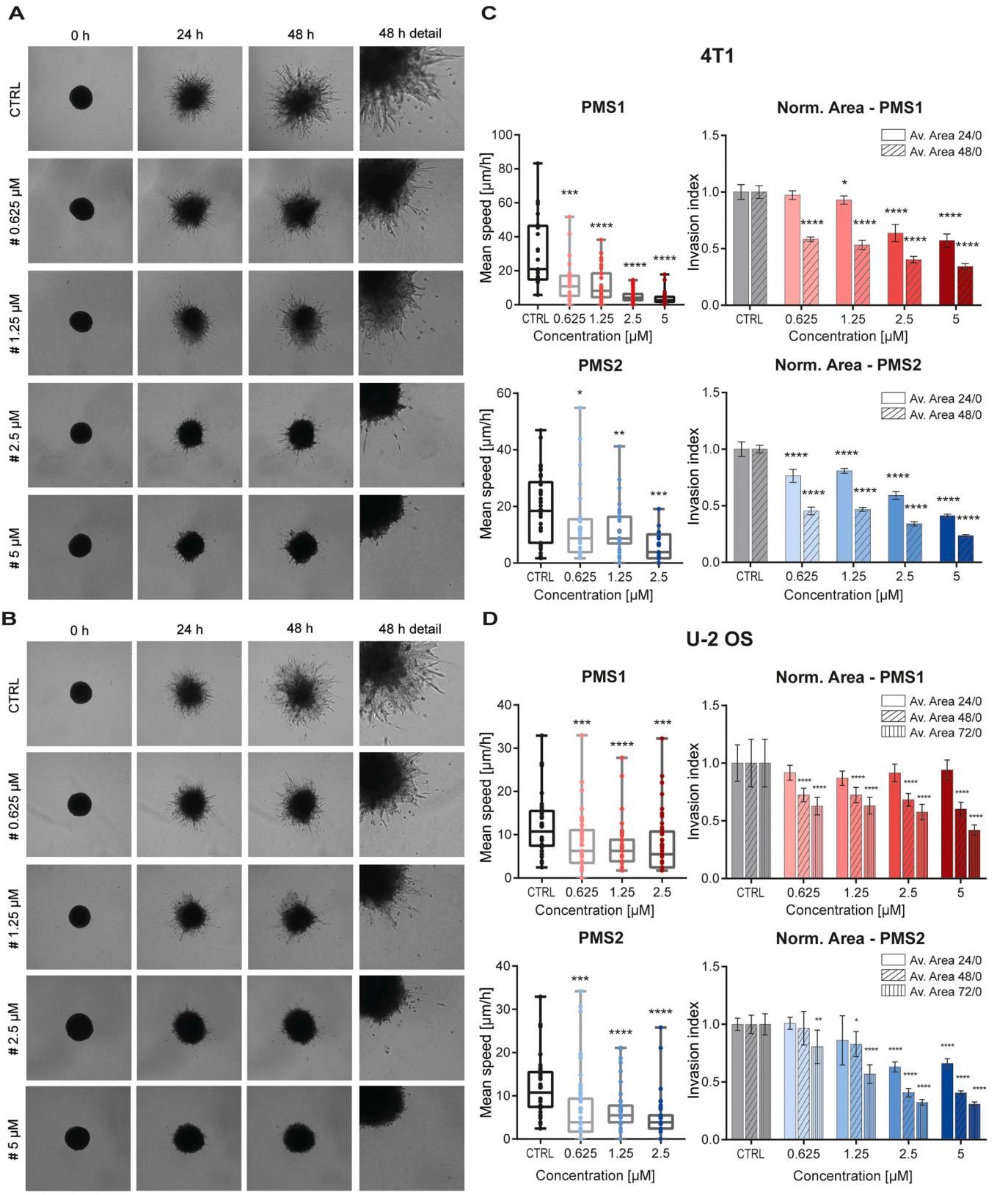

Fig. 6. 3D spheroid assay. **A-B.** 3D cell culture spheroids formed from 2500 4T1 cells were treated with different concentrations (0–5 µM) of PMS1 (A) and PMS2 (B) and captured after 24 h and 48 h of treatment, respectively. **C-D.** One-hour interval time-lapse images of spheroids were used to track the speed of cell invasion after PMS treatment. The box plot graph shows a mean of single-cell invasion velocities after 48 h of PMS treatment. Invasion index was calculated for each condition after 24 h and 48 h of treatment, respectively (bar graph).

in vitro and in mice models, yet the phase I clinical trial (NCT03404726) was terminated due to the lack of sufficient clinical benefit. Therefore, it is important to look for other agents targeting DHODH that have clinical potential.

In this study, we tested pentamethinium salts as mitochondria-targeting agents with inhibitory effects on DHODH-dependent respiration as well as exhibiting imaging capability and migrastatic potential in cancer cells. Pentamethinium salts were previously shown to be potent photosensitizers inducing mitochondrial disintegration and apoptosis upon red light illumination [36]. Accordingly, both salts (PMS1 and PMS2) turned out to be highly cytotoxic when exposed to red light (650 nm). The signal of both pentamethinium salts was colocalized with the signal of MitoTracker® Green FM indicating selective accumulation of the salts in mitochondria of cancer cells (Fig. 1B). That is not surprising as both salts were designed as mitochondrial probes with high affinity to cardiolipin, an important component of IMM [26,37]. Cardiolipins present a mitochondria-specific class of lipids with a critical role in the regulation of electron transport chain activity [38], ATP synthesis [39], mitochondrial quality control [40], and apoptosis [41]. In addition, cardiolipin can stimulate the oligomerization of Drp1, which induces sequential mitochondrial fission [42]. It has been shown that many tumors differ in content or distribution of cardiolipin within mitochondrial membranes [43,44]. This could be one possible explanation why we observed PMS cytotoxicity predominantly in cancer cell lines. On the contrary, non-malignant PNT1A cells showed relative resistance to the salts (Bax/Bcl-2 ratio lower than 1 [45,46], relatively high levels of IC_{50} values). The cytotoxic effect of the salts to cancer cells was previously observed also in human malignant melanoma cells (cell line A-375) [47].

Both salts affected the ETC, attenuated respiration, mitochondrial ATP production, and caused elevated oxidative stress. ROS generation and oxidative stress were related to mitochondrial damage under many conditions [47–49]. Accordingly, mitochondrial footprint normalized to cell area was significantly decreased in cancer cell lines indicating that these cells are losing mitochondria (probably by autophagy [47]). A decrease in the number of mitochondria can diminish the oncogenic potential of cancer cells [50], and it is also reflected by a drop in cell stiffness. A similar decrease in cell stiffness was also observed due to hydrogen peroxide treatment that promotes oxidative stress [51]. Hydrogen peroxide can upregulate the expression of FUNDC1 via activation of the ERK1/2 signal to trigger mitophagy [52].

Disruption of mitochondria (inhibition of the ETC and depletion of mitochondrial membrane potential) likely induces pseudohypoxia as treatment of cancer cells with PMS was accompanied by increase in *HIF-1α* expression. HIF-1α causes up-regulation of glycolytic enzymes including pyruvate dehydrogenase kinase, which effectively induces aerobic glycolysis [53]. Accordingly, ATP production in PMS-treated cancer cells was rescued by glycolysis. Nevertheless, DHODH-dependent respiration was attenuated, which can have serious consequences for cancer cells [9]. Several studies indicate that DHODH inhibitors are more effective against malignancies, which depend on *de novo* pyrimidine synthesis. For example, PTEN-mutant cells are dependent on glutamine flux through the *de novo* pyrimidine synthesis pathway [54]. Furthermore, both PMSs caused translocation of mitochondria from the leading edge of the cell to the area around the nucleus, which can negatively affect the ability of cancer cells to migrate [55]. The DHODH inhibition was shown to suppress NF-kB activity [56]. These phenomena can partially explain the observed migrastatic and anti-invasive effects of both salts. DHODH also cooperates with mitochondrial GPX4 to block ferroptosis in the inner mitochondrial membrane by reducing ubiquinone to antioxidant ubiquinol [57].

One of the unexpected results of the PMS treatment was the increase in *SOX2* gene expression in non-malignant PNT1A cells. This gene encodes a transcription factor that is essential for maintaining pluripotency of undifferentiated embryonic stem cells and plays a role in the formation of cancer stem cells [58]. However, SOX2 has been described as a trans-activator of phosphatase and tensin homolog (PTEN), thus inhibiting phosphatidylinositol 3-kinase/ protein kinase B (PI3K/AKT)-driven cell cycle progression and potential tumorigenesis [59]. This suggests that the oncogenic potential of overexpressed SOX2 could be attenuated by functional PTEN in PNT1A cells. On the other hand, in U-2 OS cells where PTEN expression is significantly reduced [60], expression of *SOX2* did not significantly change after PMS treatment. PC-3 cells have a homozygous deletion of the PTEN gene and are therefore negative for PTEN expression [61]. A 2-fold increase in the expression of *SOX2* was observed in PC-3 cells treated with the salts. Based on these findings, it may be plausible to test combination of PMS with SOX2 inhibitors as a combinatorial treatment of cancer. For example, EGFR inhibitors (Gefitinib and Erlotinib) and Src inhibitor (Dasatinib) reduced the levels of SOX2 by blocking the EGFR/SRC/AKT pathway. A small molecular inhibitor of LSD1 (CBB1007) or the cationic triphenylmethane pharmacophore gentian violet (GV) significantly reduced SOX2 expression and suppressed growth of cancer cells. Neddylation inhibitor (MLN4924 or Pevonedistat) effectively depleted SOX2 via targeting the FBXW2-MSX2 axis and is currently in phase II clinical trials for anti-neoplastic application [62].

Due to the central role of mitochondria in metabolism, drugs that target mitochondrial functions are likely to be toxic. Interestingly, both salts show a unique combination of specific mitochondrial localization, high affinity for DHODH, and selective cytotoxic effect against cancer cells, therefore they appear to be highly promising. However, their possible side effects and effects on the immune system need to be carefully evaluated in further studies.

5. Conclusions

In this study we showed that pentamethinium salts accumulate in mitochondria of cancer cells and have a strong effect on their mitochondria, suppressing cancer cell proliferation and migration. This is probably linked to the strong inhibitory effect of the PMS salts on DHODH-dependent respiration that has a key role in the *de novo* pyrimidine synthesis. We also showed that PMS cause redistribution of mitochondria, oxidative stress, and a decrease in mitochondria mass accompanied by a drop in cell stiffness. Due to the central role of mitochondria in metabolism, drugs that target mitochondrial functions are likely to be toxic. Interestingly, although the PMS salts accumulate in the mitochondria of all tested cells, both PMSs show selective cytotoxic effect against cancer cells, therefore they appear to be highly promising. DHODH inhibition was originally used in the treatment of rheumatoid arthritis and multiple sclerosis, but also seems to be promising for cancer therapy. In conclusion, pentamethinium salts present novel anti-cancer agents worthy of further studies.

CRediT authorship contribution statement

Jindriska Leischner Fialova: Conceptualization, Data curation, Methodology, Validation, Visualization, Writing – original draft. **Katerina Hönigova:** Conceptualization, Data curation, Methodology, Validation, Visualization, Writing – original draft. **Martina Raudenska:** Conceptualization, Data curation, Methodology, Writing – original draft. **Lucie Miksatkova:** Data curation, Investigation, Methodology, Validation. **Renata Zobalova:** Data curation, Investigation, Methodology, Validation. **Jiri Navratil:** Data curation, Investigation, Methodology, Validation. **Jana Šmigová:** Data curation, Investigation, Methodology, Validation. **Taraka Ramji Moturu:** Data curation, Software, Investigation, Methodology, Validationi, Tomas Vicar Methodology, Validation. **Jan Balvan:** Data curation, Investigation, Methodology, Validation. **Katerina Vesela:** Methodology, Data curation. **Nikita Abramenko:** Validation, Data curation. **Zdenek Kejik:** Investigation, Data curation. **Robert Kaplanek:** Data curation. **Jaromir Gumulec:** Methodology, Validation, Writing – review & editing. **Daniel Rosel:** Investigation, Resources, Supervision, Visualization, Writing –

review & editing. **Pavel Martasek:** Investigation, Resources, Supervision, Visualization, Writing – review & editing. **Jan Brábek:** Funding acquisition, Investigation, Supervision, Writing – review & editing. **Milan Jakubek:** Funding acquisition, Investigation, Supervision, Writing – review & editing. **Jiri Neuzil:** Funding acquisition, Investigation, Supervision, Writing – review & editing. **Michal Masarik:** Funding acquisition, Investigation, Project administration, Resources, Software, Supervision, Visualization, Writing – review & editing.

Conflict of interest statement

No potential conflict of interest was reported by the authors.

Data Availability

Data will be made available on request.

Acknowledgement

This work was supported by the project of Charles University in Prague [SVV260521; UNCE 204064; Cooperatio Program, research area Medical Diagnostics and Basic Medical Sciences; Progress Q26–38/LF1 and Q27/LF1], the Ministry of Education, Youth and Sports grant no. LM2018133 (EATRIS-CZ). The research was also funded by the Ministry of Industry and Trade of Czech Republic within the project No. FV40120 as well as by the Technology Agency of the Czech Republic within the projects No. TN01000013 and FW02020128, by the Ministry of Health of the Czech Republic (grant no. NU21–08-00407), by funds from Specific University Research Grant, as provided by the Ministry of Education, Youth and Sports of the Czech Republic in the year 2022 (MUNI/A/1391/2021) and by Internal Grant Agency of Masaryk university (MUNI/IGA/0954/2021) and by Czech Science Foundation (grant no. 20-05942S and 21-04607X). We also acknowledge Operational Programme Research, Development and Education, within the projects: Center for Tumor Ecology—Research of the Cancer Microenvironment Supporting Cancer Growth and Spread (reg. No. CZ.02.1.01/0.0/0.0/16_019/0000785). The project National Institute for Cancer Research (Programme EXCELES, ID Project No. LX22NPO5102) - Funded by the European Union - Next Generation EU. We acknowledge the core facility CELLIM supported by MEYS CR (LM2018129 Czech-BioImaging).

Appendix A. Supporting information

Supplementary data associated with this article can be found in the online version at doi:10.1016/j.biopha.2022.113582.

References

[1] C. Robert, A decade of immune-checkpoint inhibitors in cancer therapy, Nat. Commun. 11 (1) (2020) 3801, https://doi.org/10.1038/s41467-020-17670-y.
[2] R.L. Siegel, K.D. Miller, H.E. Fuchs, A. Jemal, Cancer statistics, 2022, CA: A Cancer J. Clin. 72 (1) (2022) 7–33, https://doi.org/10.3322/caac.21708.
[3] C.-N. Qian, Y. Mei, J. Zhang, Cancer metastasis: issues and challenges, Chin. J. Cancer 36 (1) (2017) 38, https://doi.org/10.1186/s40880-017-0206-7.
[4] V. Gogvadze, S. Orrenius, B. Zhivotovsky, Mitochondria in cancer cells: what is so special about them? Trends Cell Biol. 18 (4) (2008) 165–173, https://doi.org/10.1016/j.tcb.2008.01.006.
[5] J.S. Modica-Napolitano, J.R. Aprille, Delocalized lipophilic cations selectively target the mitochondria of carcinoma cells, Adv. Drug Deliv. Rev. 49 (1–2) (2001) 63–70, https://doi.org/10.1016/s0169-409x(01)00125-9.
[6] J. Neuzil, L.-F. Dong, J. Rohlena, J. Truksa, S.J. Ralph, Classification of mitocans, anti-cancer drugs acting on mitochondria, Mitochondrion 13 (3) (2013) 199–208, https://doi.org/10.1016/j.mito.2012.07.112.
[7] W.H. Koppenol, P.L. Bounds, C.V. Dang, Otto Warburg's contributions to current concepts of cancer metabolism, Nat. Rev. Cancer 11 (5) (2011) 325–337, https://doi.org/10.1038/nrc3038.
[8] M.G. Vander Heiden, L.C. Cantley, C.B. Thompson, Understanding the warburg effect: the metabolic requirements of cell proliferation, Science 324 (5930) (2009) 1029–1033, https://doi.org/10.1126/science.1160809.
[9] M. Bajzikova, J. Kovarova, A.R. Coelho, S. Boukalova, S. Oh, K. Rohlenova, D. Svec, S. Hubackova, B. Endaya, K. Judasova, et al., Reactivation of dihydroorotate dehydrogenase-driven pyrimidine biosynthesis restores tumor growth of respiration-deficient cancer cells, e10, Cell Metab. 29 (2) (2019) 399–416, https://doi.org/10.1016/j.cmet.2018.10.014.
[10] G.L. Oliveira, A.R. Coelho, R. Marques, P.J. Oliveira, Cancer cell metabolism: rewiring the mitochondrial hub, Biochim. Biophys. Acta Mol. Basis Dis. 1867 (2) (2021), 166016, https://doi.org/10.1016/j.bbadis.2020.166016.
[11] S.Y. Lunt, M.G. Vander Heiden, Aerobic glycolysis: meeting the metabolic requirements of cell proliferation, Annu. Rev. Cell Dev. Biol. 27 (1) (2011) 441–464, https://doi.org/10.1146/annurev-cellbio-092910-154237.
[12] J.B. Spinelli, H. Yoon, A.E. Ringel, S. Jeanfavre, C.B. Clish, M.C. Haigis, Metabolic recycling of ammonia via glutamate dehydrogenase supports breast cancer biomass, Science 358 (6365) (2017) 941–946, https://doi.org/10.1126/science.aam9305.
[13] L.B. Sullivan, D.Y. Gui, M.G. Vander Heiden, Altered metabolite levels in cancer: implications for tumour biology and cancer therapy, Nat. Rev. Cancer 16 (11) (2016) 680–693, https://doi.org/10.1038/nrc.2016.85.
[14] V.S. LeBleu, J.T. O'Connell, K.N. Gonzalez Herrera, H. Wikman, K. Pantel, M. C. Haigis, F.M. de Carvalho, A. Damascena, L.T. Domingos Chinen, R.M. Rocha, et al., PGC-1α mediates mitochondrial biogenesis and oxidative phosphorylation in cancer cells to promote metastasis, 1–15, Nat. Cell Biol. 16 (10) (2014) 992–1003, https://doi.org/10.1038/ncb3039.
[15] T.V. Denisenko, A.S. Gorbunova, B. Zhivotovsky, Mitochondrial involvement in migration, invasion and metastasis, Front. Cell Dev. Biol. 7 (2019) 355, https://doi.org/10.3389/fcell.2019.00355.
[16] A.S. Tan, J.W. Baty, L.-F. Dong, A. Bezawork-Geleta, B. Endaya, J. Goodwin, M. Bajzikova, J. Kovarova, M. Peterka, B. Yan, et al., Mitochondrial genome acquisition restores respiratory function and tumorigenic potential of cancer cells without mitochondrial DNA, Cell Metab. 21 (1) (2015) 81–94, https://doi.org/10.1016/j.cmet.2014.12.003.
[17] H. Kong, C.R. Reczek, G.S. McElroy, E.M. Steinert, T. Wang, D.M. Sabatini, N. S. Chandel, Metabolic determinants of cellular fitness dependent on mitochondrial reactive oxygen species, Sci. Adv. 6 (45) (2020) eabb7272, https://doi.org/10.1126/sciadv.abb7272.
[18] S.T. Diepstraten, M.A. Anderson, P.E. Czabotar, G. Lessene, A. Strasser, G.L. Kelly, The manipulation of apoptosis for cancer therapy using BH3-mimetic drugs, Nat. Rev. Cancer 22 (1) (2022) 45–64, https://doi.org/10.1038/s41568-021-00407-4.
[19] J.R. Molina, Y. Sun, M. Protopopova, S. Gera, M. Bandi, C. Bristow, T. McAfoos, P. Morlacchi, J. Ackroyd, A.-N.A. Agip, et al., An inhibitor of oxidative phosphorylation exploits cancer vulnerability, Nat. Med. 24 (7) (2018) 1036–1046, https://doi.org/10.1038/s41591-018-0052-4.
[20] S. Hubackova, R. Zobalova, M. Dubisova, J. Smigova, S. Dvorakova, K. Korinkova, Z. Ezrova, B. Endaya, K. Blazkova, E. Vlcak, et al., Simultaneous targeting of mitochondrial metabolism and immune checkpoints as a new strategy for renal cancer therapy, Clin. Transl. Med (2022), https://doi.org/10.1002/ctm2.645.
[21] D.R. Evans, H.I. Guy, Mammalian pyrimidine biosynthesis: fresh insights into an ancient pathway, J. Biol. Chem. 279 (32) (2004) 33035–33038, https://doi.org/10.1074/jbc.R400007200.
[22] S. Boukalova, S. Hubackova, M. Milosevic, Z. Ezrova, J. Neuzil, J. Rohlena, Dihydroorotate dehydrogenase in oxidative phosphorylation and cancer, Biochim. Biophys. Acta Mol. Basis Dis. 1866 (6) (2020), 165759, https://doi.org/10.1016/j.bbadis.2020.165759.
[23] Y. Zhou, L. Tao, X. Zhou, Z. Zuo, J. Gong, X. Liu, Y. Zhou, C. Liu, N. Sang, H. Liu, et al., DHODH and cancer: promising prospects to be explored, Cancer Metab. 9 (1) (2021) 22, https://doi.org/10.1186/s40170-021-00250-z.
[24] J.T. Madak, A. Bankhead, C.R. Cuthbertson, H.D. Showalter, N. Neamati, Revisiting the role of dihydroorotate dehydrogenase as a therapeutic target for cancer, Pharmacol. Ther. 195 (2019) 111–131, https://doi.org/10.1016/j.pharmthera.2018.10.012.
[25] T. Bříza, J. Králová, B. Dolenský, S. Rimpelová, Z. Kejík, T. Ruml, M. Hajdúch, P. Džubák, I. Mikula, P. Martásek, et al., Striking antitumor activity of a methinium system with incorporated quinoxaline unit obtained by spontaneous cyclization, Chembiochem 16 (4) (2015) 555–558, https://doi.org/10.1002/cbic.201402662.
[26] T. Bříza, J. Králová, S. Rimpelová, M. Havlík, R. Kaplánek, Z. Kejík, P. Martásek, I. Mikula, P. Džubák, M. Hajdúch, et al., Pentamethinium salts as ligands for cancer: sulfated polysaccharide co-receptors as possible therapeutic target, Bioorg. Chem. 82 (2019) 74–85, https://doi.org/10.1016/j.bioorg.2018.02.011.
[27] B.P. Dranka, G.A. Benavides, A.R. Diers, S. Giordano, B.R. Zelickson, C. Reily, L. Zou, J.C. Chatham, B.G. Hill, J. Zhang, et al., Assessing bioenergetic function in response to oxidative stress by metabolic profiling, Free Radic. Biol. Med. 51 (9) (2011) 1621–1635, https://doi.org/10.1016/j.freeradbiomed.2011.08.005.
[28] G. Bitencourt-Ferreira, W.F. de Azevedo Jr., Exploring the scoring function space, Methods Mol. Biol. 2053 (2019) 275–281, https://doi.org/10.1007/978-1-4939-9752-7_17.
[29] R. Thomsen, M.H. Christensen, MolDock: a new technique for high-accuracy molecular docking, J. Med. Chem. 49 (11) (2006) 3315–3321, https://doi.org/10.1021/jm051197e.
[30] Z. Ul-Haq, W. Khan, S. Kalsoom, F.L. Ansari, In silico modeling of the specific inhibitory potential of thiophene-2,3-dihydro-1,5-benzothiazepine against BChE in the formation of β-amyloid plaques associated with alzheimer's disease, Theor. Biol. Med. Model. 7 (1) (2010) 22, https://doi.org/10.1186/1742-4682-7-22.
[31] E.F. Pettersen, T.D. Goddard, C.C. Huang, G.S. Couch, D.M. Greenblatt, E.C. Meng, T.E. Ferrin, UCSF chimera—a visualization system for exploratory research and analysis, J. Comput. Chem. 25 (13) (2004) 1605–1612, https://doi.org/10.1002/jcc.20084.
[32] J.A. Prescher, C.R. Bertozzi, Chemistry in living systems, Nat. Chem. Biol. 1 (1) (2005) 13–21, https://doi.org/10.1038/nchembio0605-13.

[33] Y. Park, C. Depeursinge, G. Popescu, Quantitative phase imaging in biomedicine, Nat. Photonics 12 (10) (2018) 578–589, https://doi.org/10.1038/s41566-018-0253-x.
[34] Y. Ma, L. Wang, R. Jia, The role of mitochondrial dynamics in human cancers, Am. J. Cancer Res 10 (5) (2020) 1278–1293.
[35] A.P. Trotta, J.E. Chipuk, Mitochondrial dynamics as regulators of cancer biology, Cell. Mol. Life Sci. 74 (11) (2017) 1999–2017, https://doi.org/10.1007/s00018-016-2451-3.
[36] R. Krejcir, T. Briza, M. Sterba, O. Simoncik, P. Muller, P.J. Coates, P. Martasek, B. Vojtesek, P. Zatloukalova, Anticancer pentamethinium salt is a potent photosensitizer inducing mitochondrial disintegration and apoptosis upon red light illumination, J. Photochem. Photobiol. B: Biol. 209 (2020), 111939, https://doi.org/10.1016/j.jphotobiol.2020.111939.
[37] T. Bříza, S. Rimpelová, J. Králová, K. Záruba, Z. Kejík, T. Ruml, P. Martásek, V. Král, Pentamethinium fluorescent probes: the impact of molecular structure on photophysical properties and subcellular localization, Dyes Pigments 107 (2014) 51–59, https://doi.org/10.1016/j.dyepig.2013.12.021.
[38] M. Fry, D.E. Green, Cardiolipin requirement for electron transfer in complex i and iii of the mitochondrial respiratory chain, J. Biol. Chem. 256 (4) (1981) 1874–1880.
[39] T.H. Haines, N.A. Dencher, Cardiolipin: a proton trap for oxidative phosphorylation, FEBS Lett. 528 (1–3) (2002) 35–39, https://doi.org/10.1016/S0014-5793(02)03292-1.
[40] C.T. Chu, J. Ji, R.K. Dagda, J.F. Jiang, Y.Y. Tyurina, A.A. Kapralov, V.A. Tyurin, N. Yanamala, I.H. Shrivastava, D. Mohammadyani, et al., Cardiolipin externalization to the outer mitochondrial membrane acts as an elimination signal for mitophagy in neuronal cells, Nat. Cell Biol. 15 (10) (2013) 1197–1205, https://doi.org/10.1038/ncb2837.
[41] Z.T. Schug, E. Gottlieb, Cardiolipin acts as a mitochondrial signalling platform to launch apoptosis, Biochim. Et. Biophys. Acta (BBA) - Biomembr. 1788 (10) (2009) 2022–2031, https://doi.org/10.1016/j.bbamem.2009.05.004.
[42] N. Stepanyants, P.J. Macdonald, C.A. Francy, J.A. Mears, X. Qi, R. Ramachandran, Cardiolipin's propensity for phase transition and its reorganization by dynamin-related protein 1 form a basis for mitochondrial membrane fission, MBoC 26 (17) (2015) 3104–3116, https://doi.org/10.1091/mbc.E15-06-0330.
[43] M.A. Kiebish, X. Han, H. Cheng, J.H. Chuang, T.N. Seyfried, Cardiolipin and electron transport chain abnormalities in mouse brain tumor mitochondria: lipidomic evidence supporting the warburg theory of cancer, J. Lipid Res. 49 (12) (2008) 2545–2556, https://doi.org/10.1194/jlr.M800319-JLR200.
[44] S.T. Ahmadpour, K. Mahéo, S. Servais, L. Brisson, J.-F. Dumas, Cardiolipin, the mitochondrial signature lipid: implication in cancer, Int. J. Mol. Sci. 21 (21) (2020), https://doi.org/10.3390/ijms21218031.
[45] S. Salakou, D. Kardamakis, A.C. Tsamandas, V. Zolota, E. Apostolakis, V. Tzelepi, P. Papathanasopoulos, D.S. Bonikos, T. Papapetropoulos, T. Petsas, et al., Increased Bax/Bcl-2 ratio up-regulates caspase-3 and increases apoptosis in the thymus of patients with myasthenia gravis, Vivo 21 (1) (2007) 123–132.
[46] M. Raisova, A.M. Hossini, J. Eberle, C. Riebeling, C.E. Orfanos, C.C. Geilen, T. Wieder, I. Sturm, P.T. Daniel, The Bax/Bcl-2 ratio determines the susceptibility of human melanoma cells to CD95/Fas-mediated apoptosis, J. Invest. Dermatol. 117 (2) (2001) 333–340, https://doi.org/10.1046/j.0022-202x.2001.01409.x.
[47] R. Krejcir, L. Krcova, P. Zatloukalova, T. Briza, P.J. Coates, M. Sterba, P. Muller, J. Kralova, P. Martasek, V. Kral, et al., A cyclic pentamethinium salt induces cancer cell cytotoxicity through mitochondrial disintegration and metabolic collapse, Int. J. Mol. Sci. 20 (17) (2019), https://doi.org/10.3390/ijms20174208.
[48] D.R. Green, G. Kroemer, The pathophysiology of mitochondrial cell death, Science 305 (5684) (2004) 626, https://doi.org/10.1126/science.1099320.
[49] M. Cano Sanchez, S. Lancel, E. Boulanger, R. Neviere, Targeting oxidative stress and mitochondrial dysfunction in the treatment of impaired wound healing: a systematic review, Antioxidants 7 (8) (2018), https://doi.org/10.3390/antiox7080098.
[50] A. Panov, Z. Orynbayeva, Bioenergetic and antiapoptotic properties of mitochondria from cultured human prostate cancer cell lines PC-3, DU145 and LNCaP, PLoS One 8 (8) (2013), e72078, https://doi.org/10.1371/journal.pone.0072078.
[51] S. Sun, S. Wong, A. Mak, M. Cho, Impact of oxidative stress on cellular biomechanics and rho signaling in C2C12 myoblasts, J. Biomech. 47 (15) (2014) 3650–3656, https://doi.org/10.1016/j.jbiomech.2014.09.036.
[52] L. Hui, H. Wu, T.-W. Wang, N. Yang, X. Guo, X.-J. Jang, Hydrogen peroxide-induced mitophagy contributes to laryngeal cancer cells survival via the upregulation of FUNDC1, Clin. Transl. Oncol. 21 (5) (2019) 596–606, https://doi.org/10.1007/s12094-018-1958-5.
[53] J. Kim, I. Tchernyshyov, G.L. Semenza, C.V. Dang, HIF-1-mediated expression of pyruvate dehydrogenase kinase: a metabolic switch required for cellular adaptation to hypoxia, Cell Metab. 3 (3) (2006) 177–185, https://doi.org/10.1016/j.cmet.2006.02.002.
[54] D. Mathur, E. Stratikopoulos, S. Ozturk, N. Steinbach, S. Pegno, S. Schoenfeld, R. Yong, V.V. Murty, J.M. Asara, L.C. Cantley, et al., PTEN regulates glutamine flux to pyrimidine synthesis and sensitivity to dihydroorotate dehydrogenase inhibition, Cancer Discov. 7 (4) (2017) 380–390, https://doi.org/10.1158/2159-8290.CD-16-0612.
[55] B. Cunniff, A.J. McKenzie, N.H. Heintz, A.K. Howe, AMPK activity regulates trafficking of mitochondria to the leading edge during cell migration and matrix invasion, MBoC 27 (17) (2016) 2662–2674, https://doi.org/10.1091/mbc.E16-05-0286.
[56] S.B. Ng, K.J. Buckingham, C. Lee, A.W. Bigham, H.K. Tabor, K.M. Dent, C.D. Huff, P.T. Shannon, E.W. Jabs, D.A. Nickerson, et al., Exome sequencing identifies the cause of a mendelian disorder, Nat. Genet. 42 (1) (2010) 30–35, https://doi.org/10.1038/ng.499.
[57] C. Mao, X. Liu, Y. Zhang, G. Lei, Y. Yan, H. Lee, P. Koppula, S. Wu, L. Zhuang, B. Fang, et al., DHODH-mediated ferroptosis defence is a targetable vulnerability in cancer, Nature 593 (7860) (2021) 586–590, https://doi.org/10.1038/s41586-021-03539-7.
[58] O. Leis, A. Eguiara, E. Lopez-Arribillaga, M.J. Alberdi, S. Hernandez-Garcia, K. Elorriaga, A. Pandiella, R. Rezola, A.G. Martin, Sox2 expression in breast tumours and activation in breast cancer stem cells, Oncogene 31 (11) (2012) 1354–1365, https://doi.org/10.1038/onc.2011.338.
[59] S. Wang, J. Tie, R. Wang, F. Hu, L. Gao, W. Wang, L. Wang, Z. Li, S. Hu, S. Tang, et al., SOX2, a predictor of survival in gastric cancer, inhibits cell proliferation and metastasis by regulating PTEN, Cancer Lett. 358 (2) (2015) 210–219, https://doi.org/10.1016/j.canlet.2014.12.045.
[60] Jiawen Feng, Yaping Dang, Weiqi Zhang, Xuyang Zhao, Cong Zhang, Zhiyuan Hou, Yan Jin, A. McNutt Michael, R. Marks Andrew, Yuxin Yin, PTEN arginine methylation by PRMT6 suppresses PI3K–AKT signaling and modulates Pre-MRNA splicing, Proc. Natl. Acad. Sci. 116 (14) (2019) 6868–6877, https://doi.org/10.1073/pnas.1811028116.
[61] M. Fraser, H. Zhao, K.R. Luoto, C. Lundin, C. Coackley, N. Chan, A.M. Joshua, T. A. Bismar, A. Evans, T. Helleday, et al., PTEN deletion in prostate cancer cells does not associate with loss of RAD51 function: implications for radiotherapy and chemotherapy, Clin. Cancer Res. 18 (4) (2012) 1015–1027, https://doi.org/10.1158/1078-0432.CCR-11-2189.
[62] S. Zhang, Y. Sun, Targeting oncogenic SOX2 in human cancer cells: therapeutic application, Protein Cell 11 (2) (2020) 82–84, https://doi.org/10.1007/s13238-019-00673-x.